Stability and Dynamic Analysis of PMSG-based Wind Generation System Considering Torsional Oscillation and Virtual Inertia Control

Yizhuo Ma, *Graduate Student Member*, *IEEE*, Jin Xu, *Senior Member*, *IEEE*, Guojie Li, and Keyou Wang, *Member*, *IEEE*

***Abstract*—Most permanent magnet synchronous generator (PMSG) based wind generation systems currently employ grid-following control, relying on a phase-locked loop (PLL) for grid connection. However, it leads to a lack of inertia support in the system. To address this, the virtual inertia control (VIC) is crucial for improvement, yet it introduces potential instability due to torsional oscillation interaction with PLL and low-frequency oscillations, which is an underexplored area. This paper presents a comprehensive analysis of the grid-connected PMSG-based wind generation system. It confirms the necessity of employing a full-order model for studying stability on the quasi-electromechanical timescale (QET) by a comparison with the reduced-order model. Then, a comprehensive modal analysis is conducted to analyze the effect of VIC parameters, shaft inertia time constant, PLL parameters, and torsional oscillation damping (TOD) controller gain on the interaction of QET oscillations under two typical control strategies. The occurrence of interaction and mode conversion is observed when the oscillation frequency and root loci of the torsional, PLL, and low-frequency oscillations are close. Finally, a theoretical analysis is validated via simulation verification in Simulink. These findings offer a valuable guidance for industrial PMSG applications considering VIC.**

***Index Terms*—Permanent magnet synchronous generator (PMSG), grid-following control, torsional oscillation, virtual inertia control (VIC), phase-locked loop (PLL), modal analysis.**

I. Introduction

In recent years, the permanent magnet synchronous generator (PMSG) based wind generation system has rapidly evolved and emerged as a prominent power source in the double-high (i.e., high penetration of renewable energy plus high penetration of power electronic equipment) power system [1], [2]. Most PMSG-based wind generation systems adopt grid-following control, which exhibits the following characteristics: ① operating as a current source in the power system; ② utilizing a phase-locked loop (PLL) to synchronize with the power system; and ③ lacking inertia/frequency support capability [3]. In the context of a low-inertia power grid with an increasing proportion of renewable energy, it becomes necessary to implement virtual inertia control (VIC) to provide inertia and frequency support for the power grid [4]. VIC enables the PMSG to participate in power grid frequency regulation and improve the system frequency characteristics. However, it also has a significant impact on the dynamic characteristics and system stability [5].

Based on Fig. 1, the oscillations of the grid-connected PMSG-based wind generation system with grid-following control can be classified into two main categories: ① system-level oscillation, which includes inter-area and local oscillations; and ② equipment-level oscillation, which includes PLL and torsional oscillations.

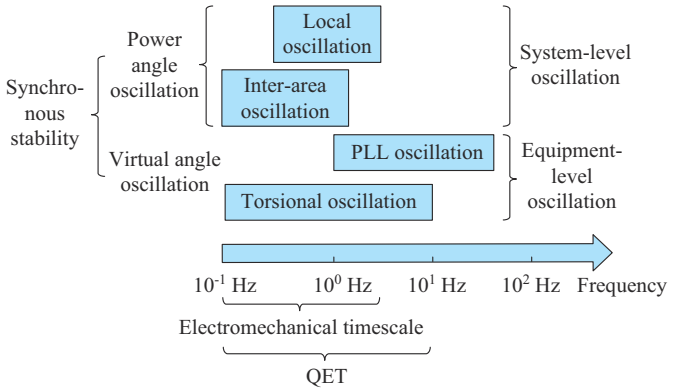

Fig. 1. Dynamic characteristics of grid-connected PMSG-based wind generation system.

The frequency range of the equipment-level oscillation is quite broad, mainly determined by the PLL parameters and the constant time of shaft inertia. The introduction of VIC may result in interaction between these oscillation modes. It is important to note that the frequency range of these modes are close and coinciding. When assessing the system stability, the range of electromechanical timescale is insufficient. Thus, this paper suggests expanding the concept of electro-

Manuscript received: March 16, 2024; revised: June 2, 2024; accepted: August 14, 2024. Date of CrossCheck: August 14, 2024. Date of online publication: October 15, 2024.

This work was supported by the National Key R&D Program of China (No. 2022YFB2402800).

Y. Ma, J. Xu (corresponding author), G. Li, and K. Wang are with the Key Laboratory of Control of Power Transmission and Conversion Ministry of Education, Shanghai Jiao Tong University, Shanghai, China (e-mail: 925998709@sjtu.edu.cn; xujin20506@sjtu.edu.cn; liguojie@sjtu.edu.cn; wangkeyou@sjtu.edu.cn).

DOI: 10.35833/MPCE.2024.000573

mechanical timescale to quasi-electromechanical timescale (QET), which includes the frequency range of torsional oscillation.

Table I provides a summary and comparison of recent studies [6]-[16]. The difference of type 1 and type 2 is detailed in Section II-C.

TABLE I
SUMMARY AND COMPARISON OF RECENT STUDIES

Reference	WT generator	Control strategy	VIC	Torsional oscillation	PLL oscillation	Model type
[6]	PMSG	Type 1	√	√		Reduced-order
[7]	PMSG	Types 1 and 2		√		Full-order
[8]	PMSG	Type 1			√	Full-order
[9]	PMSG	Type 2		√		Full-order
[10]	PMSG	Type 1		√		Full-order
[11]	PMSG	Type 1	√		√	Reduced-order
[12]	PMSG	Type 1	√		√	Full-order
[13]	DFIG		√	√		Full-order
[14]	DFIG		√		√	Reduced-order
[15]	DFIG		√		√	Reduced-order
[16]	DFIG		√	√		Reduced-order
This paper	PMSG	Types 1 and 2	√	√	√	Full-order

Note: DFIG is short for doubly-fed induction generator; and the symbol √ represents that the VIC, torsional oscillation, or PLL oscillation is considered in the corresponding reference.

It is concluded that the impact of the interactions introduced by VIC includes two aspects.

The first aspect is that the introduction of VIC negatively affects the torsional oscillation damping (TOD) [6], [13], [16]. In [6], the mechanism and influencing factors of torsional oscillation are explored in the PMSG-based wind generation system with VIC using the reduced-order model. It is concluded that when the differential coefficient exceeds $4H$, which represents the total inertia of the system, the shafting damping exhibits a negative value. In [13], an adaptive damping control method based on reactive power modulation is proposed to suppress the torsional oscillation with the implementation of VIC. In [16], the reason for the reduction of shafting damping after the introduction of VIC is investigated based on the transfer function of electromagnetic torque and generator speed for the DFIG. The literature reviewed suggests that the first research gap is the oversimplification of the modeling used in studying the impact of VIC on shafting stability of PMSG-based wind generation systems. This simplification may introduce errors and potentially lead to incorrect findings. Additionally, the lack of mechanism explanation further undermines the validity of the results.

The second aspect is that the VIC channel allows for the interaction between the PMSG-based wind generation system and power grid, resulting in the coupling among the torsional, PLL, and low-frequency oscillations in the QET. Consequently, the characteristics of the electromechanical oscillations, primarily influenced by the synchronous generators (SGs), may be altered, significantly affecting the dynamic characteristics and system stability. In [7], the interaction between torsional and power oscillations is analyzed based on the full-order model of a PMSG-based wind generation system connected to the IEEE 39-bus power system through modal analysis. In [12], the impact of grid-connected PMSG-based wind generation system on the electromechanical oscillation modes of power system is studied, considering the effects of PLL based on the interconnected model of the power system. In [15], the impact of DFIG with VIC on the small-signal stability of the system caused by the PLL is investigated, revealing that the coupling between DFIG and SGs is mainly affected by PLL and VIC. The second research gap is that the existing research on PLL dynamics and system stability with VIC lacks consideration of the impact of torsional oscillation on system stability and the interaction among torsional, PLL, and system-level oscillations through the VIC channel. This interaction may significantly alter the dynamic characteristics of the system.

To address the research gaps, this study initially develops both full-order and reduced-order small-signal models for the PMSG-based wind farm (WF) connected to the four-machine two-area (FMTA) system. It compares the frequency error and damping ratio error of QET oscillation between the two models, demonstrating the necessity of the full-order model for analyzing the stability of QET oscillations. Furthermore, the transfer function of electromagnetic torque and speed difference for PMSG with VIC is derived using the damping torque method, explaining the detrimental impact of VIC on TOD. Next, a comprehensive modal analysis is carried out to examine the effect of VIC parameters, shaft inertia time constant, PLL parameters, and TOD controller gain on the interaction of QET oscillations under two typical control strategies. In this paper, the occurrence of interaction and mode conversion is observed when the oscillation frequencies and root loci of the torsional, PLL, and low-frequency oscillations are close.

In conclusion, the main contributions of this paper are as follows.

1) Investigating two typical control strategies involving torsional oscillation and VIC in PMSG-based wind genera-

tion systems.

2) Demonstrating the necessity for small-signal analysis using full-order model.

3) Theoretically deducing the mechanism leading to the degradation of shafting damping due to the introduction of VIC.

4) Investigating and analyzing a potential novel stability problem involving the interaction and mode conversion among torsional, PLL, and low-frequency oscillations in high-proportion grid-following power systems with the introduction of VIC.

The rest of this paper is organized as follows. Section II focuses on the modelling and control of the grid-connected PMSG-based wind generation system. Section III presents the stability, dynamic, and modal analysis of the model developed in Section II. The time-domain simulation results are illustrated in Section IV. Finally, the conclusions are provided in Section V.

II. Modelling and Control of Grid-connected PMSG-based Wind Generation System

The typical topology of grid-connected PMSG-based wind generation system, as depicted in Fig. 2, comprises various components: wind turbine (WT), shaft system, PMSG, back-to-back full-power converter, transformers, grid-side converter (GSC) control section, machine-side converter (MSC) control section, and grid-connected line. This section introduces a mathematical model of the considered system in Fig. 2 using the per-unit system, where MPPT is short for maximum power point tracking; PCC is short for point of coulping conection; and PI is short for proportional-integral. The PLL oscillation couples with the machine-side dynamics through the VIC, and the PLL detects the q-axis PCC voltage u_{gq} to couple with inter-area oscillation and local oscillation.

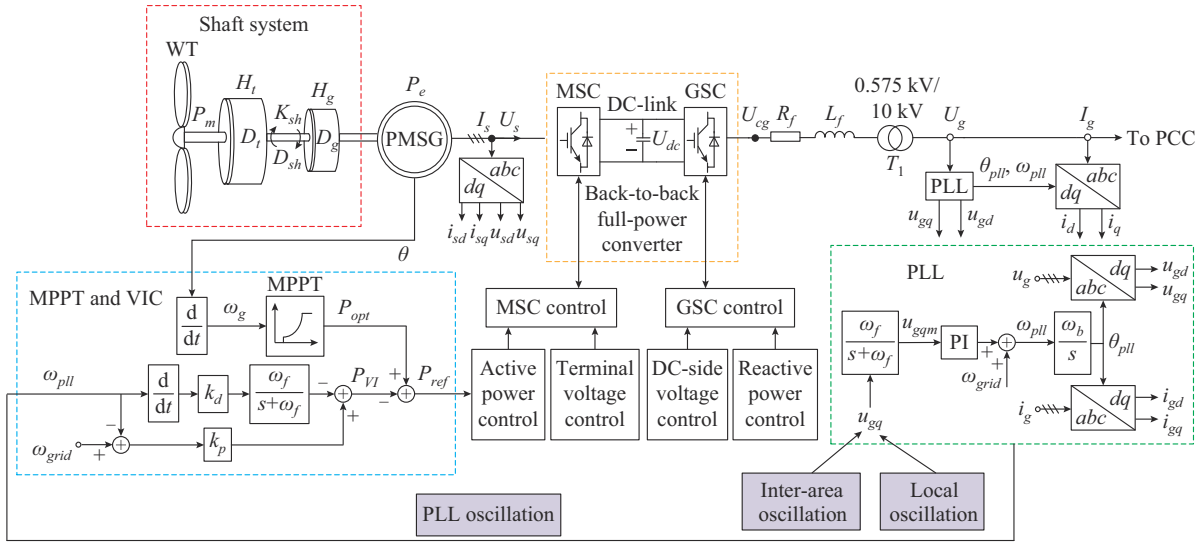

Fig. 2. Typical topology of grid-connected PMSG-based wind generation system.

A. PMSG Model

The PMSG is controlled in d-q rotating coordinates, aligning the d-axis with the magnetic flux linkage of rotor ψ_f. The stator voltage is expressed as [17]:

$$\begin{cases} u_{sd} = -R_s i_{sd} - \dfrac{L_d}{\omega_{eb}} \dfrac{\mathrm{d}i_{sd}}{\mathrm{d}t} + \omega_g L_q i_{sq} \\ u_{sq} = -R_s i_{sq} - \dfrac{L_d}{\omega_{eb}} \dfrac{\mathrm{d}i_{sq}}{\mathrm{d}t} - \omega_g L_d i_{sd} + \omega_g \psi_f \end{cases} \tag{1}$$

where u_{sd} and u_{sq} are the d- and q-axis stator terminal voltages, respectively; i_{sd} and i_{sq} are the d- and q-axis stator currents, respectively; R_s is the PMSG stator resistance; ω_{eb} is the base value of stator angular frequency; ω_g is the angular velocity of generator rotor; and L_d and L_q are the d- and q-axis self-inductances of PMSG stator, respectively.

B. Shaft System Model

The double-mass model is adopted to describe the dynamic characteristics of shaft system [18], which can be expressed as:

$$\begin{cases} 2H_t \dfrac{\mathrm{d}\omega_t}{\mathrm{d}t} = T_m - T_{sh} \\ 2H_g \dfrac{\mathrm{d}\omega_g}{\mathrm{d}t} = T_{sh} - T_e \\ \dfrac{\mathrm{d}\theta_{sh}}{\mathrm{d}t} = \omega_{eb}(\omega_t - \omega_g) \\ T_{sh} = K_{sh}\theta_{sh} + D_{sh}(\omega_t - \omega_g) \end{cases} \tag{2}$$

where H_t and H_g are the inertial time constants of WT and PMSG mass blocks, respectively; ω_t is the WT speed of generator rotor; θ_{sh} is the torsion angle of WT relative to generator rotor; K_{sh} is the stiffness coefficient of shaft system; D_{sh} is the damping coefficient of shaft system; and T_m, T_e, and T_{sh} are the mechanical, electromagnetic, and shaft system torques, respectively.

C. Control Strategy

This study focuses on two typical control strategies, as shown in Fig. 3(a) and (b), respectively.

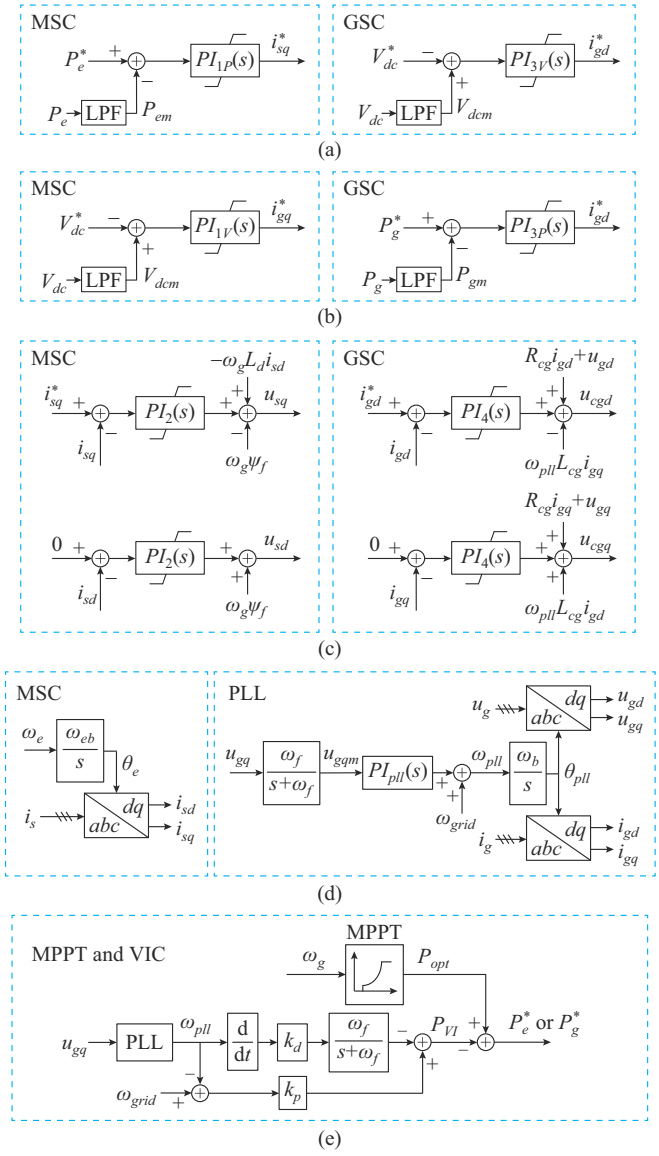

Fig. 3. Different control structures. (a) Type 1. (b) Type 2. (c) Reactive power and current control of MSC and GSC. (d) Coordinate transformation of MSC and PLL. (e) MPPT and VIC.

1) Type 1: MSC regulates the electromagnetic power of PMSG, and GSC regulates the DC-link voltage.

2) Type 2: MSC regulates the DC-link voltage, and GSC modulates the output active power.

Type 1 is the most commonly-used control strategy. However, since it controls active power on the machine side, the application of VIC can lead to interactions and mode conversions among torsional, PLL, and low-frequency oscillations, which deteriorates the shaft damping. Type 2 has better fault ride-through performance during unsymmetrical grid faults and is also widely used [9]. Therefore, it does not lead to interactions and mode conversions among torsional, PLL, and low-frequency oscillations when VIC is applied, but it still deteriorates shaft damping. Hence, it is necessary to study the system stability under the two control strategies.

In Fig. 3, P_e^* and P_e are the reference and actual active power on the machine side, respectively; V_{dc}^* and V_{dc} are the reference and actual DC-link voltages, respectively; P_g^* and P_g are the reference and actual active power on the grid side, respectively; R_{cg} and L_{cg} are the grid resistance and inductance, respectively; i_{sq}^* is the q-axis reference stator current; i_{gd}^* and i_{gd} are the d-axis reference and actual currents on the grid side, respectively; u_{cgd} and u_{cgq} are the d- and q-axis GSC voltages, respectively; u_{gd} is the d-axis PCC voltage; the subscript m denotes the output of the variable after passing through an LPF; ω_{pll} is the detected grid frequency obtained by PLL; $PI_{1P}(s)=K_{p1P}+K_{i1P}/s$, and K_{p1P} and K_{i1P} are the proportional and integral coefficients of the power outer loop for MSC, respectively; $PI_{1V}(s)=K_{p1V}+K_{i1V}/s$, and K_{p1V} and K_{i1V} are the proportional and integral coefficients of the voltage outer loop for MSC, respectively; $PI_2(s)=K_{p2}+K_{i2}/s$, and K_{p2} and K_{i2} are the proportional and integral coefficients of the current inner loop for MSC, respectively; $PI_{3P}(s)=K_{p3P}+K_{i3P}/s$, and K_{p3P} and K_{i3P} are the proportional and integral coefficients of the power outer loop for GSC, respectively; $PI_{3V}(s)=K_{p3V}+K_{i3V}/s$, and K_{p3V} and K_{i3V} are the proportional and integral coefficients of the voltage outer loop for GSC, respectively; $PI_4(s)=K_{p4}+K_{i4}/s$, and K_{p4} and K_{i4} are the proportional and integral coefficients of the current inner loop for MSC, respectively; θ_{pll} is the phase of u_g based on the dq-frame of PLL; ω_{grid} is the reference grid frequency; ω_b is the base value of grid angular velocity; θ_e is the rotation angle of PMSG; and $PI_{pll}(s)=K_{p,pll}+K_{i,pll}/s=K_{p,pll}+x_{pll}$, and $K_{p,pll}$ and $K_{i,pll}$ are the proportional and integral coefficients of PI controller for the PLL, respectively; P_{opt} is the reference active power with MPPT; and P_{VI} is the reference active power with VIC.

As shown in Fig. 3(d), the PLL parameters are expressed as:

$$\begin{cases} u_{gqm}=\dfrac{\omega_f}{s+\omega_f}u_{gq} \\ \omega_{pll}=PI_{pll}(s)\cdot u_{gqm}+\omega_{grid} \\ \theta_{pll}=\omega_b\omega_{pll}/s \end{cases} \tag{3}$$

The parameter values can be found in Supplementary Material A Table SAI.

Figure 3(e) shows the structure of MPPT and VIC. The active power references P_e^* and P_g^* can be expressed as:

$$P_e^*=P_g^*=\begin{cases} k_{opt}\omega_g^3+k_p(\omega_{grid}-\omega_{pll})+k_d(\omega_{grid}-\omega_{pll})s & 0<\omega_g<\omega_{\max} \\ P_{\max} & \omega_g\geq\omega_{\max} \end{cases} \tag{4}$$

where k_{opt} is the MPPT curve coefficient; $P_{\max}$ is the maximum active power output of PMSG; $\omega_{\max}$ is the maximun angular velocity of generator rotor; k_p is the ratio coefficient of VIC; and k_d is the differential coefficient of VIC.

The model of a PMSG-based WF connected to the FMTA system is utilized to study the stability and dynamic performances of QET oscillations with VIC, as shown in Fig. 4. The WF comprises 350 PMSGs, each rated at 2 MW. For the streamline analysis, the WF model is simplified to an aggregated model of a single PMSG-based wind generation

system [19]. The parameters for the PMSG-based wind generation system are available in Supplementary Material A Table SAI, while those for the AC grid and SGs are provided in Supplementary Material B Table SBI. The linearized model, which incorporates electromagnetic transients, is formulated as the full-order model. In Supplementary Materials C and D, the detailed linearization models of PMSG-based wind generation system and AC grid are presented.

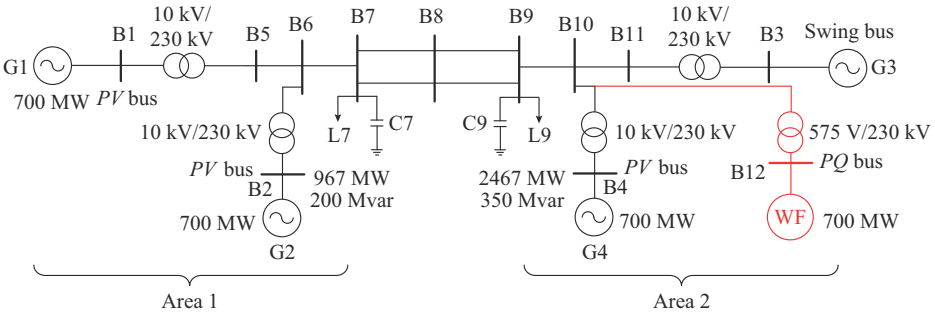

Fig. 4. Model of PMSG-based WF connected to FMTA system.

III. Stability, Dynamic, and Modal Analysis

A. Verification of Necessity for Full-order Model

The reduced-order model of the grid-connected PMSG-based wind generation system with VIC emphasizes electromechanical transient characteristics with a large time constant, omitting electromagnetic transient characteristics of the PMSG and SGs. A comparison between the full-order and reduced-order models is presented in Table II.

TABLE II
Comparison of Full-order and Reduced-order Models

Component	Characteristic	
	Full-order model	Reduced-order model
Shaft system	√	√
VIC	√	√
MPPT	√	√
PMSG	√	
Outer loop control	√	
Inner loop control	√	
SG	Fourth-order model	Second-order model

Note: √ represents the dynamics of the corresponding component are considered.

The power balance relationship with the reduced-order model can be expressed as:

$$\sum_{i=1}^{n} P_{e,i} + P_w = P_{load} \tag{5}$$

$$\sum_{i=1}^{n} Q_{e,i} + Q_w = Q_{load} \tag{6}$$

where $P_{e,i}$ and $Q_{e,i}$ are the active power and reactive power of the i^{th} SG, respectively; n is the total number of SGs; P_w and Q_w are the active power and reactive power of WF, respectively, $P_w = k_{opt}\omega_g^3 + k_p(\omega_{grid} - \omega_{pll}) + k_d(\omega_{grid} - \omega_{pll})s$, and $Q_w = Q_w^*$; and P_{load} and Q_{load} are the active power and reactive power of load in AC grid, respectively.

Based on the parameters in Tables SAI and SBI, the modal analysis yields eigenvalues and damping ratios for the full-order and reduced-order models of the QET oscillation modes, as shown in Table III. The QET oscillations are categorized into five main modes.

1) Local oscillation mode of area 1 dominated by the SGs in area 1 (mode 1).

2) Local oscillation mode of area 2 dominated by the SGs in area 2 (mode 2).

3) Torsional oscillation mode dominated by the shaft system (mode 3).

4) PLL oscillation mode dominated by the PLL (mode 4).

5) Inter-area oscillation mode dominated by all SGs (mode 5).

TABLE III
QET Oscillation Modes with Full-order and Reduced-order Models

Mode	Full-order model		Reduced-order model		Major state variables	Error (%)	
	Eigenvalue	Damping ratio (%)	Eigenvalue	Damping ratio (%)		Frequency	Damping ratio
1	−0.34 ± j14.17	4.32	−0.08 ± j15.57	0.51	ω_{g1}, θ_{g1}, ω_{g2}, θ_{g2}	9.9	88.2
2	−0.39 ± j17.59	4.95	−0.13 ± j18.77	0.71	ω_{g3}, θ_{g3}, ω_{g4}, θ_{g4}	6.7	85.6
3	−0.35 ± j16.04	2.21	−0.35 ± j16.03	2.43	θ_{sh}, ω_g	0	0.1
4	−0.97 ± j13.92	9.99	−1.10 ± j13.59	8.08	x_{pll}, θ_{pll}	13.2	33.0
5	−0.27 ± j3.86	44.07	−0.17 ± j4.52	3.46	ω_{g1}, θ_{g1}, ω_{g2}, θ_{g2} ω_{g3}, θ_{g3}, ω_{g4}, θ_{g4}	17.1	92.1

Note: θ_g represents the rotor angle of the SG; and the subscripts 1-4 of the major state variables are the Nos. of SGs.

Varying PLL parameters impact the PLL oscillation frequency and damping ratio, potentially causing error variations. We keep $K_{p,pll}$ constant at 1.1 s^{-1} while incrementally increasing $K_{i,pll}$ from 100 to 290 s^{-1} with a step size of 10 s^{-1}. The damping ratio error and frequency error are shown in Figs. 5 and 6, respectively. The root loci of oscillation modes with reduced-order and full-order models are given in Fig. 7. In modes 1 and 2, the frequency error and damping ratio error remain relatively stable. In mode 3, the damping ratio error gradually increases by 6.8% with the increase of $K_{i,pll}$, reaching as high as 78%, while the frequency error remains close to zero. In mode 4, the frequency error initially decreases and then increases, so does the damping ratio error. In mode 5, the damping ratio error gradually decreases to 41%, while the frequency error remains within 10%.

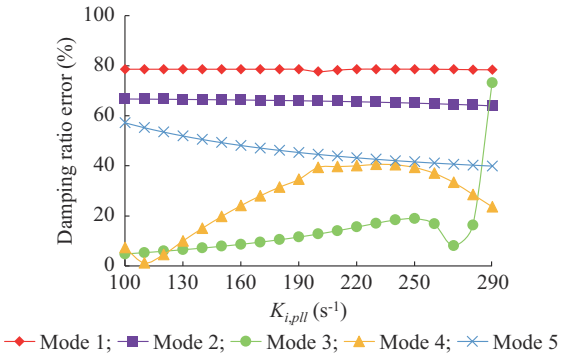

Fig. 5. Damping ratio error with various $K_{i,pll}$.

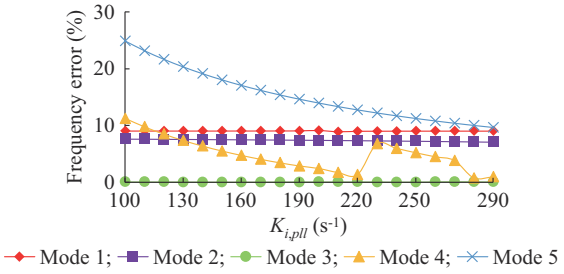

Fig. 6. Frequency error with various $K_{i,pll}$.

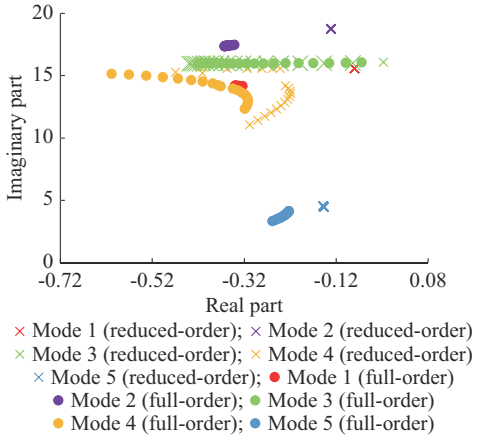

Fig. 7. Root locus of oscillation modes with reduced-order and full-order models.

For modes 1, 2, and 5, the rotor winding transients in the fourth-order model significantly impact their damping ratio and frequency. We obtain the relevant normalized participation factors (NPFs) in mode 4 with both reduced-order and full-order models. The NPFs in mode 4 associated with local oscillation of area 2 and PLL oscillation are 35.17% and 47.50%, respectively. This significant difference can be attributed to the exclusion of rotor winding transients. Additionally, since the resonance can occur when the frequencies and root loci of modes 3 and 4 are close, the differences in the frequencies and root loci of mode 4 with the reduced-order and full-order models also affect the resonance between modes 4 and 3, leading to errors of mode 3 with reduced-order and full-order models.

From the above analysis, the following conclusions can be drawn.

1) The model order reduction significantly affects the damping ratio and frequency of each mode, with a difference of more than 40% an 30%, respectively.

2) Modes 1 and 2 are relatively unaffected by the influence of modes 4 and 5.

3) The model order reduction has the minimal impact on mode 3, but when the PLL oscillation frequency approaches the torsional oscillation frequency, the impact of model reduction on errors increases.

4) To obtain the accurate stability analysis results for the PMSG-based wind generation system, the full-order model should be employed.

B. Torsional Oscillation Characteristics of PMSG with VIC

According to the electromagnetic damping analysis method [20], the linearized electromagnetic torque of PMSG ΔT_e can be expressed as:

$$\Delta T_e = D_e \Delta\omega_\Delta + K_e \Delta\theta_{sh} \tag{7}$$

$$T_e = P_e/\omega_g \tag{8}$$

$$P_e - P_g = C_{dc} V_{dc} (\mathrm{d}V_{dc}/\mathrm{d}t) \tag{9}$$

$$\Delta T_e = \Delta P_e/\omega_{g0} - P_{e0}\Delta\omega_g/\omega_{g0}^2 \tag{10}$$

$$\Delta P_e = \Delta P_g + C_{dc} V_{dc0} (\mathrm{d}\Delta V_{dc}/\mathrm{d}t) \tag{11}$$

where the symbol Δ represents the linearized increments; D_e and K_e are the electrical damping coefficient and synchronization coefficient, respectively; C_{dc} is the DC-link capacitance; $\Delta\omega_\Delta$ is the speed difference between $\Delta\omega_t$ and $\Delta\omega_g$, i.e., $\Delta\omega_\Delta = \Delta\omega_t - \Delta\omega_g$; and the subscript 0 indicates the steady-state value.

It can be observed from (8)-(11) that ΔT_e mainly depends on ΔP_e, ΔP_g, and ΔV_{dc}, which affect the torsional oscillation characteristics.

According to (1) and (7), the transfer function of θ_{sh} and T_m is deduced as:

$$\frac{\Delta\theta_{sh}}{\Delta T_m} = \frac{\dfrac{\omega_{eb}}{2H_t}}{s^2 + \left(\dfrac{D_{sh}}{2H_t} + \dfrac{D_{sh}}{2H_g} - \dfrac{D_e}{2H_g}\right)s + \omega_{eb}\left(\dfrac{K_{sh}}{2H_t} + \dfrac{K_{sh}}{2H_g} - \dfrac{K_e}{2H_g}\right)} \tag{12}$$

By referring to (12), the damping attenuation factor ξ for torsional oscillation can be determined as:

$$\xi=\frac{D_{sh}(H_t+H_g)-D_eH_t}{4H_tH_g\omega_{osc}} \tag{13}$$

$$\omega_{osc}=\sqrt{\omega_{eb}\left(\frac{K_{sh}}{2H_t}+\frac{K_{sh}-K_e}{2H_g}\right)} \tag{14}$$

where ω_{osc} is the natural oscillation angular frequency of shaft system.

Based on (12) and (13), D_e exhibits a negative correlation with ξ, and K_e is the cause of torsional oscillation frequency deviation.

Without the implement of VIC, the small-signal active power of the PMSG can be determined by linearizing the MPPT curve around its steady-state operating point:

$$\Delta P_g^*=3k_{opt}\omega_{g0}^2\Delta\omega_g \tag{15}$$

In Fig. 8, the blue line represents the MPPT curves corresponding to different k_{opt} values. When the wind speed V_w remains constant and the rotor speed range is not wide, the reference values of active power with VIC (points $A1$ and $A2$ with rotor speeds of ω_{gA1} and ω_{gA2}) and without VIC (point A with rotor speeds of ω_{g0}) are approximately equal [21], so we have:

$$k_{opt}^*\omega_{gA1}^3\approx k_{opt}\omega_{g0}^3 \tag{16}$$

$$\omega_{gA1}=\omega_{g0}+2\pi\lambda\Delta f \tag{17}$$

where k_{opt}^* is the MPPT curve coefficient with VIC; λ is the speed adjustment coefficient, $\lambda=\omega_g/\omega_{pll}$; and $\Delta f=\Delta\omega_{pll}/(2\pi)$.

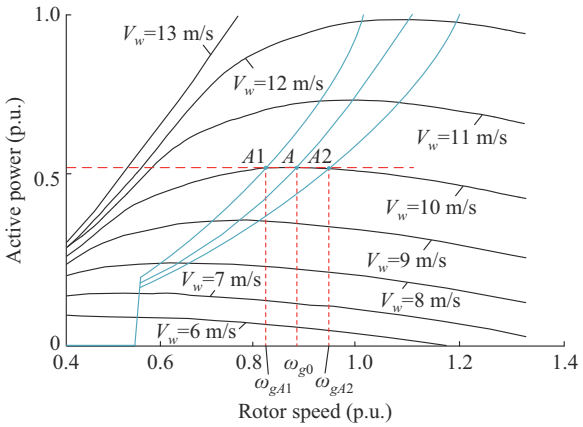

Fig. 8. Reference value of active power with VIC.

Thus, k_{opt}^* can be calculated as:

$$k_{opt}^*=\frac{\omega_{g0}^3}{(\omega_{g0}+2\pi\lambda\Delta f)^3}k_{opt} \tag{18}$$

Based on (1), (8), (18), and the active power control loop in Fig. 9, the electromagnetic torque is expressed as:

$$T_e=\psi_f i_{sq}=\psi_f\frac{k_{opt}^*n_1n_2\omega_g^3-n_1n_2T_e\omega_g}{R_s+L_qs/\omega_{eb}+n_2} \tag{19}$$

where $n_1=K_{p1P}+K_{i1P}/s$; and $n_2=K_{p2P}+K_{i2P}/s$.

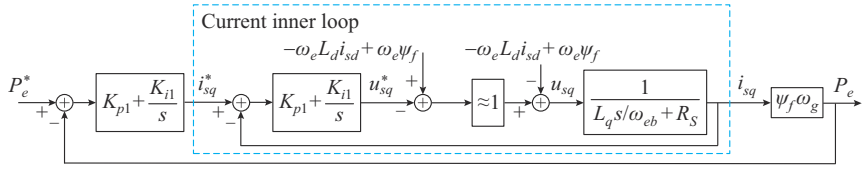

Fig. 9. Active power control loop of MSC.

By simultaneously linearizing both sides of (19), the incremental transfer function of ΔT_e and $\Delta\omega_\Delta$ can be formulated as (20). To simplify (20), we define the coefficients m and $G(s)$, whose expressions are given in (21), and ΔT_e can be expressed as (22).

$$\frac{\Delta T_e}{\Delta\omega_\Delta}=-\psi_f\frac{H_t}{H_t+H_g}\frac{\left(3k_{opt}^*\omega_{g0}^2-\frac{P_{g0}}{\omega_{g0}}\right)[K_{p1P}K_{p2}s^2+(K_{p1P}K_{i2}+K_{i1P}K_{p2})s+K_{i1P}K_{i2}]}{(L_q/\omega_b)s^3+(R_s+K_{p2}+\omega_{g0}K_{p1P}K_{p2})s^2+[K_{i2}+\omega_{g0}(K_{p1P}K_{i2}+K_{i1P}K_{p2})]s+\omega_{g0}K_{i1P}K_{i2}} \tag{20}$$

$$\begin{cases}m=2k_{opt}\omega_{g0}^2\dfrac{(\omega_{g0}-2\pi\lambda\Delta f)\omega_{g0}^2-2\pi^2\Delta f^2\lambda^2(3\omega_{g0}+4\pi\Delta f)}{(\omega_{g0}+2\pi\lambda\Delta f)^3}<2k_{opt}\omega_{g0}^2\\ G(s)=-\psi_f\dfrac{H_t}{H_t+H_g}\dfrac{K_{p1P}K_{p2}s^2+(K_{p1P}K_{i2}+K_{i1P}K_{p2})s+K_{i1P}K_{i2}}{L_qs^3+(R_s+K_{p2}+\omega_{g0}K_{p1P}K_{p2})s^2+[K_{i2}+\omega_{g0}(K_{p1P}K_{i2}+K_{i1P}K_{p2})]s+\omega_{g0}K_{i1P}K_{i2}}\end{cases} \tag{21}$$

$$\Delta T_e=mG(s)\Delta\omega_\Delta \tag{22}$$

The implementation of VIC results in a decrease in the coefficient m, which in turn leads to a negative increase in D_e. This increase in D_e reduces the shafting damping and negatively affects the system stability.

C. Effect of VIC Parameters on System Stability

The VIC parameters k_d and k_p directly affect the degree of coupling among torsional, PLL, and low-frequency oscillations. Therefore, it is essential to investigate the effect of VIC parameters on system stability. Previous studies using the reduced-order model find that the torsional oscillation instability occurs when $k_d>4H$ [6], which needs to be validated with the full-order model. This subsection analyzes the root locus and damping ratio changes with different k_p and k_d under two control strategies (types 1 and 2).

First, the influence of k_d on system stability is studied while k_p is constant at 1 p.u.. As k_d increases from 0 to 180

p.u. with a step of 1 p.u., the damping ratio and root locus are obtained, as shown in Figs. 10 and 11, respectively, under types 1 and 2. It can be observed that augmenting k_d leads to reduced damping in modes 3 and 4 while causing a rightward shift in the root locus. Remarkably, for sufficiently large k_d, the root locus tends to stabilize, resulting in non-negative shafting damping. This observation contradicts with the conclusion drawn from the reduced-order model, which incorrectly suggests that the shafting damping becomes negative when $k_d > 4H$. Nevertheless, it is noteworthy that augmenting k_d introduces additional high-frequency components, which may potentially induce system instability. To mitigate this risk, reducing the LPF bandwidth of VIC is recommended to enhance the system stability.

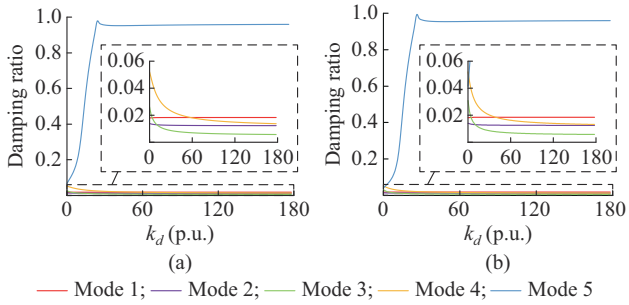

Fig. 10. Damping ratio of oscillation modes with various k_d. (a) Type 1. (b) Type 2.

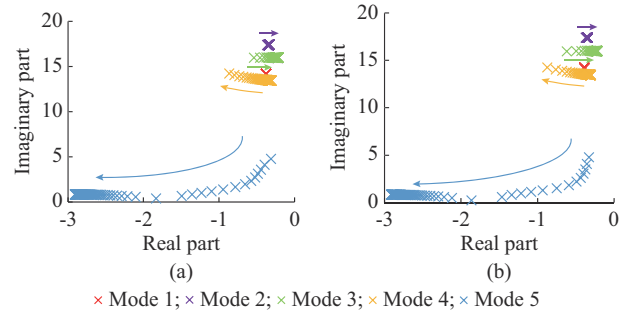

Fig. 11. Root locus of oscillation modes with various k_d. (a) Type 1. (b) Type 2.

To investigate the impact of k_p on the system stability, we maintain $k_d = 2.8$ p.u. and increase k_p from 0 to 90 p.u. with a step size of 1 p.u.. Figures 12 and 13 demonstrate that as k_p increases, the damping decreases in mode 3 and increases in mode 4. Notably, the effect of k_p on the damping of these modes remains relatively modest. Furthermore, it can be observed that simultaneously increasing both k_d and k_p notably enhances the damping of inter-area oscillation.

D. Effect of Shaft Inertia Time Constant on System Stability

Due to the uncertainty of the shaft inertia time constant H, it is necessary to consider its impact on the system stability. The following two cases are considered: ① $k_p = 0$ p.u. and $k_d = 0$ p.u. without VIC; and ② $k_p = 1$ p.u. and $k_d = 2.8$ p.u. with VIC. H is varied from 0.5 to 20 s with a step of 0.5 s.

Figures 14 and 15 show that the variations in H have the minor impact on QET oscillations expect mode 3 when VIC is not considered.

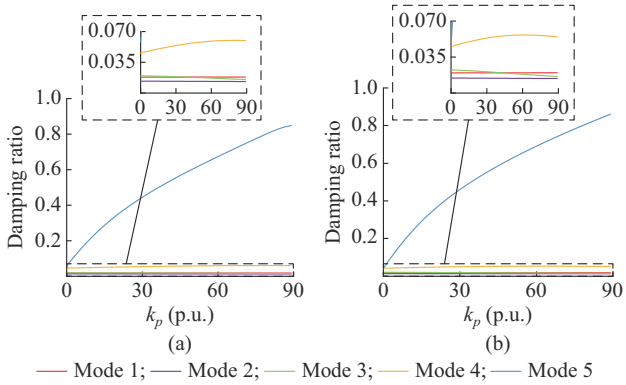

Fig. 12. Damping ratio of oscillation modes with various k_p. (a) Type 1. (b) Type 2.

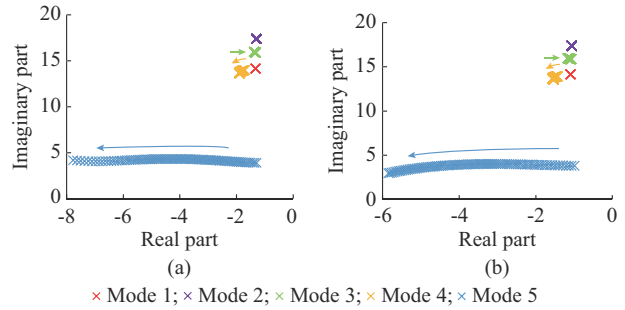

Fig. 13. Root locus of oscillation modes with various k_p. (a) Type 1. (b) Type 2.

However, when VIC is considered, the oscillation frequency of mode 3 approaches that of modes 1, 2, and 4 as H increases. The root locus of mode 3 can either attract or repel each other, resulting in resonance phenomenon. Consequently, this resonance phenomenon results in a substantial reduction in the damping ratio of one of these modes. Nevertheless, as the shafting oscillation frequency diverges from the corresponding oscillation mode, the resonance phenomenon weakens.

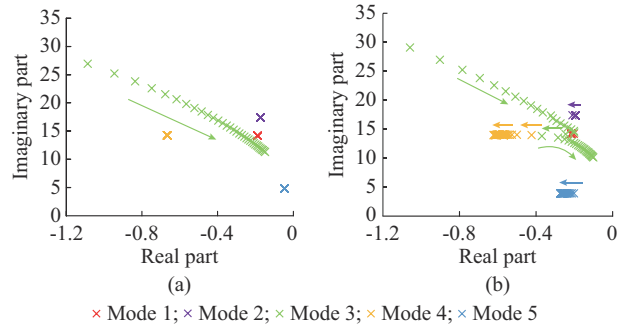

Fig. 14. Root locus of oscillation modes with various H. (a) $k_p = 0$ p.u. and $k_d = 0$ p.u. without VIC. (b) $k_p = 1$ p.u. and $k_d = 2.8$ p.u. with VIC.

The corresponding NPFs of the state variables in different modes are plotted in Fig. 16 as H varies when $k_p = 1$ p.u. and $k_d = 2.8$ p.u.. As depicted in Fig. 16, in mode 2, the NPF of the state variable associated with torsional oscillation experiences an increase as H approaches 8.5 s, peaking at 11% when $H = 8.5$ s.

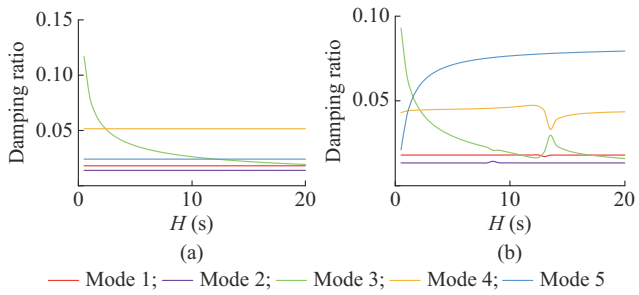

Fig. 15. Damping ratio of oscillation modes with various H. (a) $k_p=0$ p.u. and $k_d=0$ p.u. without VIC. (b) $k_p=1$ p.u. and $k_d=2.8$ p.u. with VIC.

In mode 3, the NPF of the state variable associated with local oscillation of area 2 reaches 10% when $H=8.5$ s. Furthermore, as H approaches 13 s, a comparable trend emerges for state variables associated with torsional oscillation and local oscillation of area 1, as shown in Fig. 16(a) and (c), respectively, indicating weak coupling facilitated by the PLL connection.

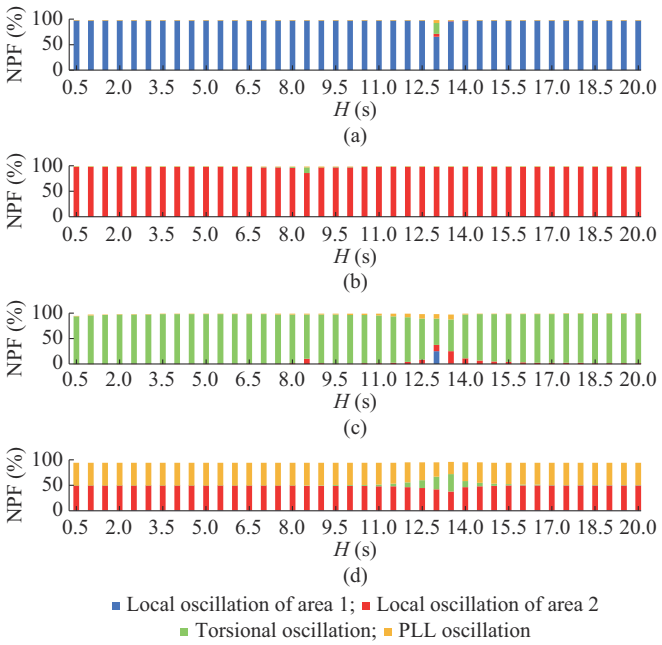

Fig. 16. NPFs of state variables in oscillation modes with various H when $k_p=1$ p.u. and $k_d=2.8$ p.u.. (a) Mode 1. (b) Mode 2. (c) Mode 3. (d) Mode 4.

According to Fig. 16(c) and (d), in mode 3, the NPFs of the state variables associated with local oscillation of area 2 and PLL oscillation experience an increase as H approaches 13.5 s. When $H=13.5$ s, they reach their maximum values, accounting for 25% and 10%, respectively. Similarly, in mode 4, the NPF of the state variable associated with the torsional oscillation accounts for 32% when $H=13.5$ s. It is evident that mode 3 and mode 4 interact significantly. Furthermore, due to this strong interaction, the NPF of the state variables associated with the local oscillation of area 2 in mode 3 increases.

E. Effect of PLL Parameter on System Stability

The change of $K_{p,pll}$ only affects the damping magnitude of mode 4, without significant effects on other modes. Therefore, the PLL bandwidth is primarily adjusted by varying $K_{i,pll}$. In this subsection, $K_{i,pll}$ increases from 100 to 500 s^{-1} in a step of 10 s^{-1} when $k_d=0$, 2, and 4 p.u..

In Fig. 17(a), when $k_d=0$ p.u., the resonance phenomenon occurs when the oscillation frequency of mode 4 approaches that of modes 2 and 3 with increased $K_{i,pll}$. With a further increase in $K_{i,pll}$, the resonance phenomenon weakens and the damping of PLL gradually decreases, eventually becoming negative. From Fig. 17(b) and (c), it can be observed that the mode conversion phenomenon takes place when $k_d=2$ p.u. and $k_d=4$ p.u., where the yellow and green numbers represent the trend of root loci with mode conversion. This phenomenon occurs when the oscillation frequency of mode 4 closely aligns with that of modes 2 and 3, significantly destabilizing the system. Besides, in Fig. 18, the interaction and influence range expand as k_d increases. When $k_d>0$, the PLL damping increases as $K_{i,pll}$ increases after the mode conversion occurring, leading to system stabilization. Moreover, with the increase of k_d, the variation range of the root locus of mode 5 decreases. As depicted in Fig. 19(c) and (d), in mode 4, the NPF of the state variable associated with torsional oscillation rises as $K_{i,pll}$ approaches 350 s^{-1}, peaking at 46% when $K_{i,pll}=350$ s^{-1}, leading to mode conversion.

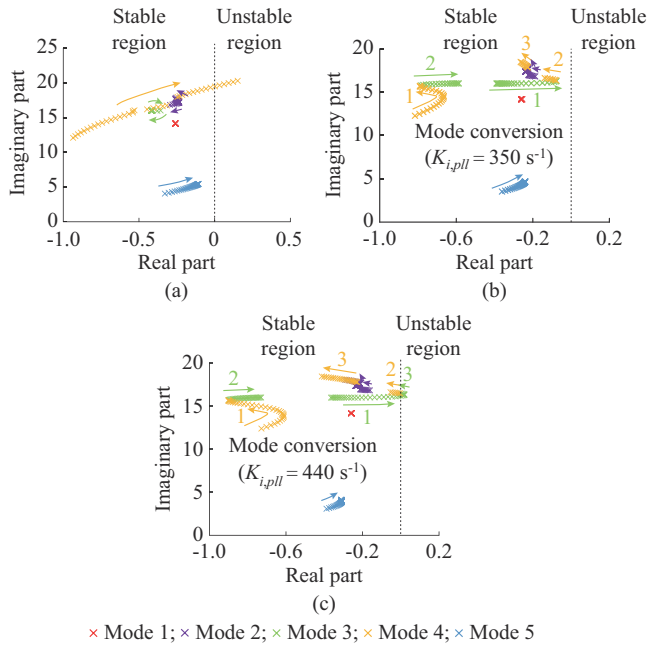

Fig. 17. Root locus of oscillation modes with various $K_{i,pll}$. (a) $k_d=0$. (b) $k_d=2$ p.u.. (c) $k_d=4$ p.u..

F. Effect of TOD Controller Gain on System Stability

To suppress the torsional oscillation, it is essential to integrate a TOD controller on the MSC. Figure 20 shows the structure of the TOD controller, where $\omega_g-\omega_t$ is the input signal of TOD controller, $y_{tod,k}$ is the output signal of TOD controller under type k; $K_{tod,k}$ is the controller gain under type k; ξ_t and ω_n are the damping ratio and center angular frequency of the band-pass filter TOD controller, respectively; and $T_{1,k}$ and $T_{2,k}$ are the time constants of the lead and lag compensators under type k, respectively. ξ_t is set to be 0.15, while ω_n is determined based on the parameters of

shaft system. The values of the time constants can be calculated using the residual method as: $T_{1,1}=0.5$ s, $T_{2,1}=0.2$ s, $T_{1,2}=-0.05$ s, and $T_{2,2}=0.01$ s.

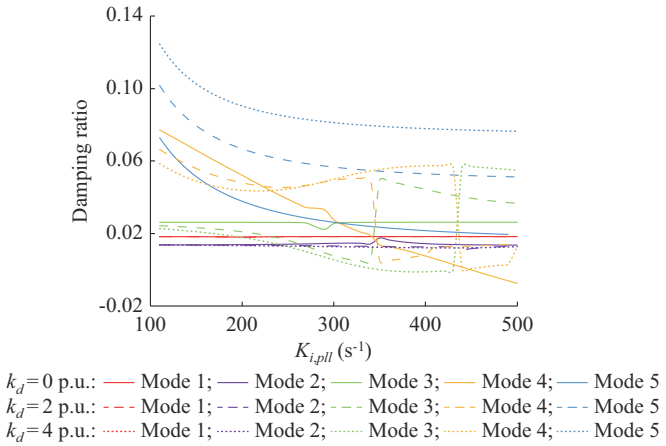

Fig. 18. Damping ratio of oscillation modes with various $K_{i,pll}$.

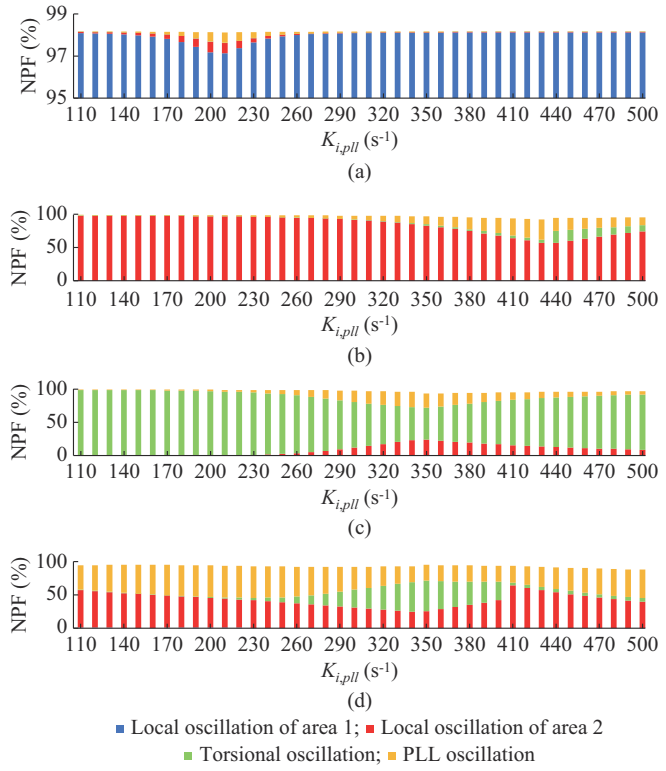

Fig. 19. NPFs of state variables in oscillation modes with various $K_{i,pll}$ when $k_d=2$ p.u.. (a) Mode 1. (b) Mode 2. (c) Mode 3. (d) Mode 4.

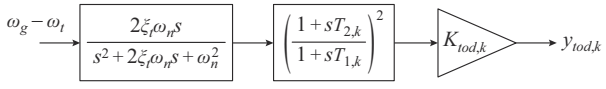

Fig. 20. Structure of TOD controller under type k.

Increasing $K_{tod,k}$ enhances the torsional oscillation suppression ability of TOD controller but introduces a new mode, denoted as mode 6. Excessive $K_{tod,k}$ values can lead to positive real roots, impacting system stability. Therefore, it is important to analyze the impact of $K_{tod,k}$ on the system stability.

In this subsection, $K_{tod,k}$ varies from 0 to 24 with a step of 0.08 under type 1 and from 0 to 150 with a step of 1 under type 2. The results in Figs. 21 and 22 show that, under type 1, as $K_{tod,1}$ increases, mode 3 and mode 6 initially converge and then gradually diverge. The damping ratio of mode 3 initially rises and then falls. The mode conversion takes place when the root locus of mode 3 approaches that of mode 4. As $K_{tod,1}$ further increases, mode 3 shifts rightward, entering an unstable region. Under type 2, mode 3 shifts rightward, entering an unstable region. When $K_{tod,2}$ reaches 40, the damping ratio reaches its maximum value. However, as $K_{tod,2}$ further increases, the root locus of mode 3 remains stable.

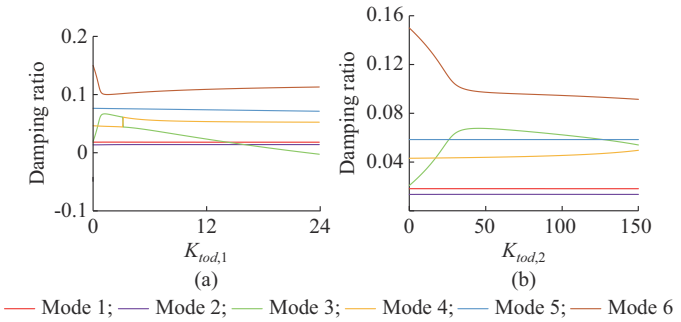

Fig. 21. Damping ratio of oscillation modes with various $K_{tod,k}$. (a) Type 1. (b) Type 2.

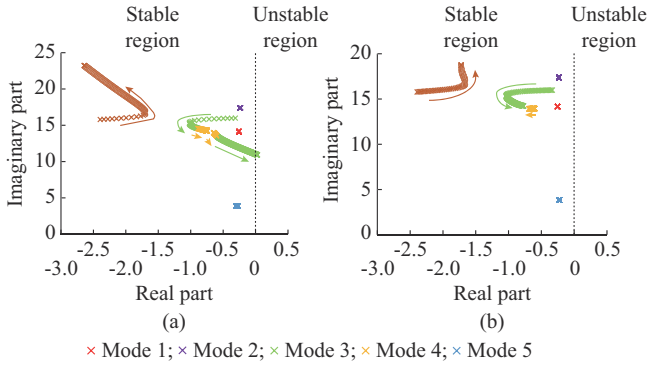

Fig. 22. Root locus of oscillation modes with various $K_{tod,k}$. (a) Type 1. (b) Type 2.

IV. Simulink Results and Discussion

To validate the prior theoretical analysis and study the dynamic performance of the PMSG-based wind generation system considering torsional oscillation and VIC, we implement the main simulation model based on Fig. 4 using the Simulink platform.

This section includes the following four simulation cases.

Case 1: three-phase short-circuit fault at B12 with rated wind speed at 12.1 m/s.

Case 2: two-phase short-circuit fault at B12 with rated wind speed at 12.1 m/s.

Case 3: three-phase short-circuit fault at B12 with 0.8 times the rated wind speed at 9.68 m/s.

Case 4: three-phase short-circuit fault at B7 with rated wind speed at 12.1 m/s.

In all four cases, the fault occurs at $t=70$ s and is cleared within 0.1 s. Due to space limitations, the necessity of considering torsional oscillation is presented in Supplementary

Material E, and the fault duration is extended to 0.2 s.

A. Verification of Effect of VIC Parameters on System Stability

This subsection examines the impact of k_d on system stability under types 1 and 2. The transient response curves in case 1 under types 1 and 2 are shown in Figs. 23 and 24, respectively, and those in cases 2 and 3 under types 1 and 2 are shown in Supplementary Material F Figs. SF1-SF4. Higher k_d values reduce the tie-line power P_{line} between areas 1 and 2 and lead to quicker attenuation in cases 1-3 due to increased inertia support provided by k_d. Additionally, from Figs. 23(c), 24(c), and SF1(c)-SF4(c), we observe that the instantaneous values of V_{dc} are higher under type 2, attributed to the DC-link voltage control on the MSC. Furthermore, Figs. 23, 24, and SF1-SF4 illustrate that increasing k_d leads to greater oscillation amplitude in ω_g and deteriorating damping. Notably, when k_d surpasses $4H$, the shaft stability is maintained, confirming the theoretical analysis.

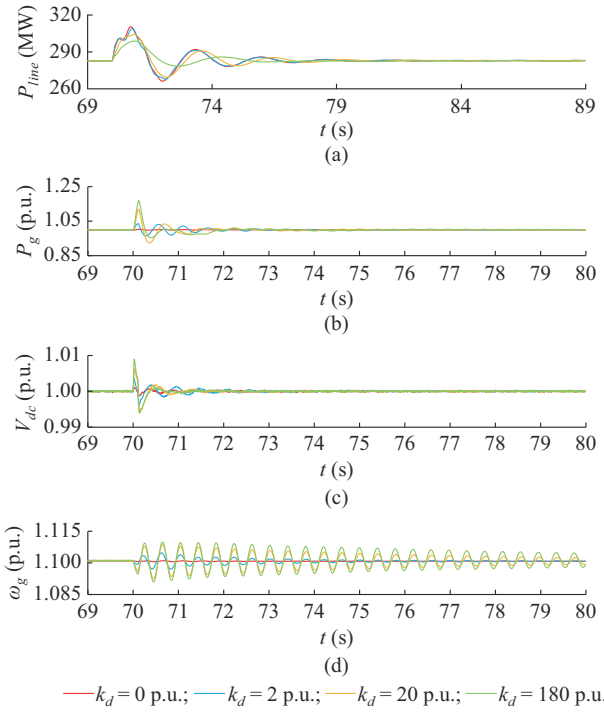

Fig. 23. Transient response curve in case 1 under type 1 with various k_d. (a) P_{line}. (b) P_g. (c) V_{dc}. (d) ω_g.

B. Verification of Effect of Shaft Inertia Time Constant on System Stability

The transient response curves under type 2 in cases 1, 2, and 4 with H of 13, 13.5, and 14 s are presented in Supplementary Material G Figs. SG1-SG3, respectively. In Figs. SG1(d)-SG3(d) and SG1(e)-SG3(e), an enhanced interaction between mode 3 and mode 4 is evident at H = 13.5 s, reducing the oscillation amplitude of ω_g and increasing the damping of mode 3. Concurrently, the oscillation amplitude of ω_{pll} increases while the damping of mode 4 decreases. Conversely, when H = 13 s and H = 14 s, the interaction between mode 3 and mode 4 weakens. Compared with H = 13.5 s, the oscillation amplitude of ω_g is larger, and the oscillation amplitude of ω_{pll} is smaller, confirming the theoretical analysis. Figures SG1(a)-(c), SG2(a)-(c), and SG3(a)-(c) reveal that the increased oscillation amplitude due to the decreased damping of mode 4 is reflected in P_{line}, P_g, and V_{dc}.

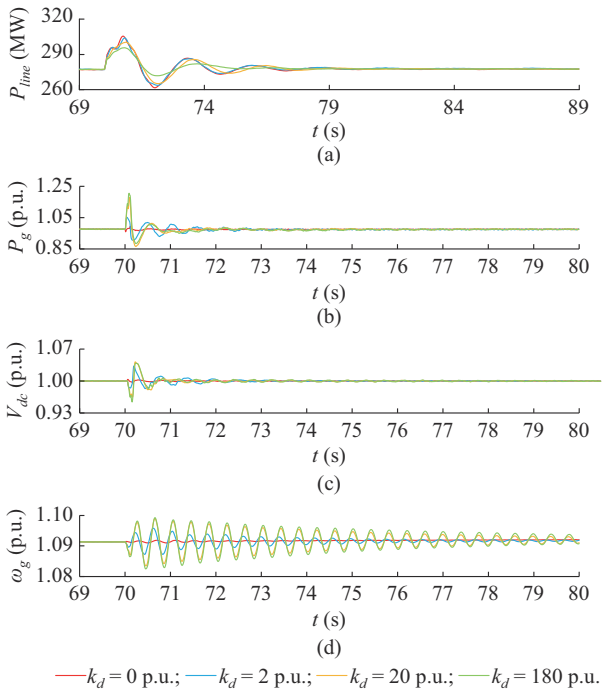

Fig. 24. Transient response curve in case 1 under type 2 with various k_d. (a) P_{line}. (b) P_g. (c) V_{dc}. (d) ω_g.

C. Verification of Effect of PLL Bandwidth on System Stability

When k_d = 4 p. u., $K_{i,pll}$ varies with values of 200, 300, 400, 800, and 1000 s^{-1}.

The transient response curves in cases 1, 2, and 4 under type 2 are presented in Supplementary Material H Figs. SH1-SH3, respectively. The modal analysis reveals that when $k_d > 0$ p.u., the mode conversation occurs in modes 3 and 4 with increasing $K_{i,pll}$. Within a specific bandwidth range, the system instability emerges. Nevertheless, as $K_{i,pll}$ further increases, the resonance diminishes, restabilizing the system.

From Figs. SH1(d)-SH3(d) and SH1(e)-SH3(e), it is evident that increasing $K_{i,pll}$ from 200 to 300 s^{-1} results in an amplified oscillation amplitude of ω_g and reduced shafting damping. Similarly, the oscillation amplitude of ω_{pll} decreases while the PLL damping intensifies. When $K_{i,pll}$ = 400 s^{-1}, ω_g and ω_{pll} diverge and oscillate, leading to system instability. Increasing $K_{i,pll}$ to 800 s^{-1} restabilizes the system. Further increasing $K_{i,pll}$ to 1000 s^{-1} leads to a decrease in the oscillation amplitude of ω_g and ω_{pll}, coupled with an increase in damping.

From Figs. SH1(a)-(c), SH2(a)-(c), and SH3(a)-(c), it can be observed that P_{line}, P_g, and V_{dc} initially experience instability followed by stability with an increase in $K_{i,pll}$. After the stability, P_{line}, P_g, and V_{dc} exhibit oscillations that synchronize with the PLL oscillation frequency, attributed to the increasing PLL bandwidth.

D. Verification of Effect of TOD Controller Gain on System Stability

This subsection concentrates on analyzing the effect of K_{tod} on system stability. The transient response curves under types 1 and 2 in cases 1, 2, and 4 are illustrated in Supplementary Material I Figs. SI1-SI6. From Figs. SI1(d)-SI3(d), it is observed that the amplitude of ω_g decreases while the damping of mode 3 increases with an increase in K_{tod}, and reaches its peak value when $K_{tod,k}=1.2$. However, when $K_{tod,k}$ increases to 20, the system becomes unstable, and ω_g diverges. Additionally, Figs. SI1(e)-SI3(e) illustrate the interaction between the PLL and torsional oscillations. It is evident that the amplitude of ω_{pll} varies with changes in $K_{tod,k}$, and this can be attributed to the interaction between mode 3 and mode 4 influenced by TOD.

As shown in Figs. SI4-SI6, increasing $K_{tod,k}$ reduces the amplitude of ω_g and gradually enhances the shafting damping. However, when $K_{tod,k}$ reaches 30, the amplitude of the initial segment of ω_g curve decreases. Despite this, the DC-link voltage instability progressively disrupts the entire system in cases 1 and 4. Under type 2, while the modal analysis indicates that the damping of mode 3 maximizes with $K_{tod,k}=40$. A high $K_{tod,k}$ can introduce instability into the DC-link voltage due to MSC control. This instability occurs because the TOD reference signal is superimposed on the DC-link voltage reference value, leading to an increase in instantaneous DC-link voltage. However, as shown in Fig. SI5, under a minor disturbance such as a two-phase short circuit, the system does not become unstable due to high instantaneous voltage values, and the attenuation rate of the ω_g curve is faster. At this point, the TOD controller performs better, which is consistent with the theoretical analysis in Section III-F.

V. Conclusion

This study provides a comprehensive analysis of a PMSG-based wind generation system. It develops both full-order and reduced-order small-signal models, and compares the frequency error and damping ratio error of QET oscillations. The results emphasize the necessity of utilizing the full-order model for stability analysis.

Furthermore, this paper derives the transfer function of ΔT_e and $\Delta\omega_\Delta$ considering VIC, using the damping torque analysis method. The theoretical analysis illustrates the detrimental effect of VIC on shaft system damping.

Moreover, a comprehensive modal analysis explores the impact of VIC parameters, shaft inertia time constant, PLL parameters, and TOD controller gain on QET oscillation interaction under two control strategies.

The key findings of this paper include:

1) The interactions among torsional, PLL, and low-frequency oscillations occur through the VIC channel when their frequencies and root loci are close.

2) Increasing k_d decreases damping in modes 3 and 4, shifting the root locus to the right. However, for sufficiently large k_d, the root locus stabilizes, and the further increase in k_d does not lead to negative shafting damping.

3) With the implementation of VIC, as H increases, the torsional oscillation mode interacts with modes 1, 2, and 4 when their oscillation frequencies are close. This interaction strengthens as VIC parameter gains rise.

4) When $k_d>0$ and the PLL bandwidth increases, a mode conversion phenomenon occurs when the PLL oscillation frequency closely aligns with the oscillation frequencies of modes 2 and 3. This effect substantially impairs system stability.

5) As K_{tod} increases, the torsional oscillation mode interacts with TOD mode when they are close.

References

[1] H. Zhang, W. Xiang, W. Lin *et al*., "Grid forming converters in renewable energy sources dominated power grid: control strategy, stability, application, and challenges," *Journal of Modern Power Systems and Clean Energy*, vol. 9, no. 6, pp. 1239-1256, Nov. 2021.

[2] G. Denis, T. Prevost, M. S. Debry *et al*., "The Migrate project: the challenges of operating a transmission grid with only inverter-based generation. A grid-forming control improvement with transient current-limiting control," *IET Renewable Power Generation*, vol. 12, no. 5, pp. 523-529, Apr. 2018.

[3] R. H. Lasseter, Z. Chen, and D. Pattabiraman, "Grid-forming inverters: a critical asset for the power grid," *IEEE Journal of Emerging and Selected Topics in Power Electronics*, vol. 8, no. 2, pp. 925-935, Jun. 2020.

[4] B. Sahu and B. P. Padhy, "Design of power system stabilizer for DFIG-based wind energy integrated power systems under combined influence of PLL and virtual inertia controller," *Journal of Modern Power Systems and Clean Energy*, vol. 12, no. 2, pp. 524-534, Mar. 2024.

[5] K. Luo, J. Guo, W. Wang *et al*., "Review of impact of grid following variable renewable energy supplementary frequency control on frequency stability and small-disturbance synchronization stability," *Proceedings of the CSEE*, vol. 43, no. 4, pp. 1262-1280, Jan. 2023.

[6] G. Wang, Q. Shi, L. Fu *et al*., "Mechanism analysis of torsional vibration for directly-driven wind turbine with permanent magnet synchronous generator shaft system with virtual inertia control," *Electric Machines and Control*, vol. 18, no. 8, pp. 8-16, Aug. 2014.

[7] Z. Zhang, X. Zhao, L. Fu *et al*., "Stability and dynamic analysis of the PMSG-based WECS with torsional oscillation and power oscillation damping capabilities," *IEEE Transactions on Sustainable Energy*, vol. 13, no. 4, pp. 2196-2210, Oct. 2022.

[8] W. Du, X. Chen, and H. Wang, "Power system electromechanical oscillation modes as affected by dynamic interactions from grid-connected PMSGs for wind power generation," *IEEE Transactions on Sustainable Energy*, vol. 8, no. 3, pp. 1301-1312, Jul. 2017.

[9] V. Ramachandran, R. Pitchaimuthu, and M. P. Selvan, "Systematized active power control of PMSG-based wind-driven generators," *IEEE Systems Journal*, vol. 14, no. 1, pp. 708-717, Mar. 2020.

[10] J. Liu, F. Zhou, C. Zhao *et al*., "Mechanism analysis and suppression strategy research on permanent magnet synchronous generator wind turbine torsional vibration," *ISA Transactions*, vol. 92, pp. 118-133, Sept. 2019.

[11] X. Wang, W. Du, and H. Wang. "Small-signal Stability of power systems as affected by D-PMSG virtual inertia control considering PLL dynamics," *Proceedings of the CSEE*, vol. 38, no. 8, pp. 2239-2252, Aug. 2018.

[12] W. Du, X. Chen, and H. Wang, "PLL-induced modal resonance of grid-connected PMSGs with the power system electromechanical oscillation modes," *IEEE Transactions on Sustainable Energy*, vol. 8, no. 4, pp. 1581-1591, Oct. 2017.

[13] X. Xi, H. Geng, G. Yang *et al*., "Torsional oscillation damping control for DFIG-based wind farm participating in power system frequency regulation," *IEEE Transactions on Industry Applications*, vol. 54, no. 4, pp. 3687-3701, Jul. 2018.

[14] X. Xu, L. Huang, Z. Wang *et al*., "Analysis on impact of virtual inertia control of DFIG-based wind turbine on electromechanical oscillation of power system," *Automation of Electric Power Systems*, vol. 43, no. 12, pp. 11-14, Aug. 2019.

[15] J. Ma, Y. Qiu, Y. Li *et al*., "Research on the impact of DFIG virtual inertia control on power system small-signal stability considering the phase-locked loop," *IEEE Transactions on Power Systems*, vol. 32, no. 3, pp. 2094-2105, May 2017.

[16] Z. Sun, H. Li, C. Liu *et al*., "Torsional oscillation damping characteristics and suppression methods of doubly-fed induction generator with virtual inertia," *Power System Technology*, vol. 45, no. 12, pp. 4671-4682, Feb. 2021.
[17] K. A. Singh and A. Chaudhary, and K. Chaudhary, "Three-phase AC-DC converter for direct-drive PMSG-based wind energy conversion system," *Journal of Modern Power Systems and Clean Energy*, vol. 11, no. 2, pp. 589-598, Mar. 2023.
[18] S. Alepuz, A. Calle, S. Busquets-Monge *et al*., "Use of stored energy in PMSG rotor inertia for low-voltage ride-through in back-to-back NPC converter-based wind power systems," *IEEE Transactions on Industrial Electronics*, vol. 60, no. 5, pp. 1787-1796, May 2013.
[19] B. Shao, S. Zhao, B. Gao *et al*., "Adequacy of the single-generator equivalent model for stability analysis in wind farms with VSC-HVDC systems," *IEEE Transactions on Energy Conversion*, vol. 36, no. 2, pp. 907-918, Jun. 2021.
[20] C. Zhang, Z. Li, Q. Gao *et al*., "Damping effects on torsional oscillation of DFIG drive-chain using different control strategies," *Proceedings of the CSEE*, vol. 33, no. 27, pp. 135-144, Sept. 2013.
[21] Y. Wang, J. Meng, X. Zhang *et al*., "Control of PMSG-based wind turbines for system inertial response and power oscillation damping," *IEEE Transactions on Sustainable Energy*, vol. 6, no. 2, pp. 565-574, Apr. 2015.

Yizhuo Ma received the B.S. degree in water conservancy and hydropower engineering from Northwest A&F University, Yangling, China, in 2019, and the M.E. degree in water conservancy engineering from Huazhong University of Science and Technology, Wuhan, China, in 2021. He is currently pursuing the Ph.D. degree in electrical engineering at Shanghai Jiao Tong University, Shanghai, China. His research interests include power system stability analysis and control considering wind power integration.

Jin Xu received the B.S. degree in electrical engineering from Sichuan University, Chengdu, China, in 2013, and the Ph.D. degree from Shanghai Jiao Tong University, Shanghai, China, in 2019. He is currently an Assistant Professor at Shanghai Jiao Tong University. His research interests include power system stability analysis, power electronic modeling, and real-time simulation.

Guojie Li received the B.Eng. and M.E. degrees in electrical engineering from Tsinghua University, Beijing, China, in 1989 and 1993, respectively, and the Ph.D. degree in electrical engineering from Nanyang Technological University, Singapore, in 1999. He was an Associate Professor with the Department of Electrical Engineering, Tsinghua University. He is currently a Professor with the Department of Electrical Engineering, Shanghai Jiao Tong University, Shanghai, China. His research interests include power system analysis and control, wind and photovoltaic (PV) power control and integration, and microgrid.

Keyou Wang received the B.S. and M.S. degrees in electrical engineering from Shanghai Jiao Tong University, Shanghai, China, in 2001 and 2004, respectively, and the Ph.D. degree from the Missouri S&T, Springfield, USA, in 2008. He is currently a Professor and Vice Department Chair of electrical engineering at Shanghai Jiao Tong University. His research interests include power system dynamic and stability, renewable energy integration, and converter dominated power system.